合金 X 射线 KES 成像中灰度与元素含量的线性关系校准

Authors: Ju, Xiao-Lu, Deng, Biao, Li, Ke, Yu, Fu-Cheng, Zhang, Hai-Peng, Xu, Ming-Wei, Du, Guo-Hao, Xie, Hong-Lan, Li, Bin, Xiao, Ti-Qiao, Xiao, Ti-Qiao

Date: 2021-12-31T14:49:25+00:00

Abstract

Doped elements in alloys significantly impact their performance. Conventional methods usually sputter the surface material of the sample, or their performance is limited to the surface of alloys owing to their poor penetration ability. The X-ray K-edge subtraction (KES) method exhibits great potential for the nondestructive in situ detection of element contents in alloys. However, the signal of doped elements usually deteriorates because of the strong absorption of the principal component and scattering of crystal grains. This in turn prevents the extensive application of X-ray KES imaging to alloys. In this study, methods were developed to calibrate the linearity between the grayscale of the KES image and element content. The methods were aimed at the sensitive analysis of elements in alloys. Furthermore, experiments with phantoms and alloys demonstrated that, after elaborate calibration, X-ray KES imaging is capable of nondestructive and sensitive analysis of doped elements in alloys.

Full Text

Calibrating the Linearity Between Grayscale and Element Content for X-ray KES Imaging of Alloys

Xiao-Lu Ju[1][2][3], Biao Deng[2], Ke Li[2], Fu-Cheng Yu[1][2][3], Hai-Peng Zhang[1][2][3], Ming-Wei Xu[1][2][3], Guo-Hao Du[2], Hong-Lan Xie[2], Bin Li[1][2][3], Ti-Qiao Xiao[1][2][3],*

[1]Shanghai Institute of Applied Physics, Chinese Academy of Sciences, Shanghai 201800, China
[2]Shanghai Synchrotron Radiation Facility, Shanghai Advanced Research Institute, Chinese Academy of Sciences, Shanghai 201204, China
[3]University of Chinese Academy of Sciences, Beijing 100049, China
*Corresponding author: xiaotiqiao@zjlab.org.cn

Abstract

Doped elements in alloys significantly impact their performance. Conventional methods typically require sputtering of the sample surface material, or are limited to surface analysis due to poor penetration capability. The X-ray K-edge subtraction (KES) method exhibits great potential for nondestructive, in situ detection of element contents in alloys. However, the signal from doped elements often deteriorates because of strong absorption by the principal component and scattering from crystal grains, which has prevented the widespread application of X-ray KES imaging to alloys. In this study, we developed methods to calibrate the linearity between the grayscale of KES images and element content, aimed at enabling sensitive elemental analysis in alloys. Experiments with phantoms and alloy samples demonstrated that after elaborate calibration, X-ray KES imaging is capable of nondestructive and sensitive analysis of doped elements in alloys.

Keywords: X-ray KES imaging; Grayscale calibration; Element analysis for alloy; Nondestructive imaging of elements

1 Introduction

The type, distribution, and content of elements in alloys significantly affect their performance, including heat resistance [1-3], machinability [3,4], strength [1,3-5], and plasticity [4,6]. Conventional techniques based on mass spectrometry or spectroscopy have been developed for elemental quantification, including laser ablation inductively coupled plasma mass spectrometry [7-9], time-of-flight secondary ion mass spectrometry [10], nanoscale secondary ion mass spectrometry [11], laser induced breakdown spectroscopy [12], and inductively coupled plasma atomic emission spectrometry [13]. However, these spectroscopic methods are destructive, typically requiring sputtering of the sample surface for composition analysis, and their repeatability cannot be guaranteed. Alternatively, nondestructive methods such as scanning electron microscopy (SEM), transmission electron microscopy (TEM), and electron probe micro-analysis (EPMA) are used to determine elemental distribution in alloys [5,14,15], but their limited penetration capability restricts analysis to the alloy surface. X-ray spectroscopy methods, including energy dispersive X-ray fluorescence (EDXRF) and X-ray photoelectron spectroscopy (XPS), are also employed for elemental analysis in alloys [16,17]. While the sensitivity of X-ray spectroscopic methods is relatively high, XPS is limited to surface detection of excited electrons.

X-ray fluorescence (XRF) spectroscopy has been extensively employed to analyze element content and distribution [18,19]. When combined with tomography, X-ray fluorescence tomography can image the three-dimensional distribution of elements in bulk samples [20-23]. In X-ray fluorescence imaging, pencil-beam scanning is typically employed to achieve spatial resolution, resulting in time-consuming data acquisition. Full-field X-ray fluorescence imaging was developed to obtain element distribution images without beam scanning [24], but the extremely low flux of X-ray fluorescence requires long exposure times to achieve sufficient signal-to-noise ratio. For rapid and efficient imaging of element distribution in alloys, an imaging strategy that shows significant differences around the K-edge of X-ray absorption for specific elements represents a promising approach.

X-ray K-edge subtraction (KES) imaging was proposed by Jacobson et al. in 1953 [25]. This technique enables full-field, in situ, and rapid imaging. The KES method has been successfully used to observe copper ion adsorption in polymer particles [26] and to achieve real-time full-field imaging of biomedical samples by illuminating with two monochromatic beams at energies before and after the K-edge of the element of interest [27,28]. In principle, the grayscale of KES images is proportional to the content of the element of interest and is commonly used to depict its spatial distribution. Bayat et al. used KES imaging gray values to observe element distribution and control inhaled gas content in biological tissues via a ventilation device for quantitative functional lung imaging [29-31]. Elleaume et al. measured contrast agent concentration based on KES image grayscale together with the theoretical attenuation coefficient of the element of interest in a biomedical phantom [32]. Furthermore, when combined with tomography, the KES method enabled three-dimensional mapping of strontium in bone with theoretical analysis based on a priori information [33].

To date, most KES applications for element evaluation have focused on biomedical samples rather than alloys. In alloys, the principal component of bulk samples dominates X-ray absorption during KES imaging, and scattering from crystal grains significantly deteriorates signals from doped elements. Consequently, the signal-to-noise ratio of KES images for specific elements is severely degraded, making direct evaluation of element content based on image grayscale difficult. Various factors affect the precision of quantitative analysis based on KES image grayscale. Specifically, noise sources—including photon shot noise, detector noise, and scattering noise—reduce the signal-to-noise ratio and affect the linearity between element content and grayscale, particularly for low element content and small mass absorption differences around the K-edge. This effect is especially significant for alloy applications where strong absorption typically produces noisy images. Additionally, subtraction between images acquired before and after the K-edge introduces further noise. For in-situ imaging of raw samples, random sample thickness can also result in inaccurate quantification of element content.

In this study, we report a series of solutions to address these problems in applying KES imaging to alloys, aiming to eliminate factors that deteriorate the linearity between element content and grayscale.

2.1 Grayscale of KES Image

K-edge subtraction X-ray imaging (KES), also termed energy subtraction technology, is based on the relationship between incident and transmitted beams

[25]:

$$I = I_0 \exp\left[-\sum_i \left(\frac{\mu}{\rho}\right)_i \rho_i d\right] \tag{1}$$

where $(\mu/\rho)_i$ denotes the mass absorption coefficients of elements, d represents X-ray penetration depth through materials, and ρ_i denotes element densities. Furthermore, (x, y) is the coordinate of the pixel of interest. As long as projections are recorded linearly by an X-ray detector, the grayscale of images is proportional to intensity. As proposed by Lehmann et al. [34], the content of element j in the sample, which is the product of density and depth, can be obtained by processing two sets of images at energies slightly above and below the K absorption edge of the element of interest:

$$G^{+}_{obj} = G^{+}_0 \exp\left[-\left(\frac{\mu}{\rho}\right)^{+}_{obj} \rho_{obj} d - \left(\frac{\mu}{\rho}\right)^{+}_{base} \rho_{base} d\right] \tag{2}$$

$$G^{-}_{obj} = G^{-}_0 \exp\left[-\left(\frac{\mu}{\rho}\right)^{-}_{obj} \rho_{obj} d - \left(\frac{\mu}{\rho}\right)^{-}_{base} \rho_{base} d\right] \tag{3}$$

where G denotes the gray value captured by a charge-coupled device (CCD) after X-rays penetrate the sample, and G_0 denotes the gray value from the X-ray beam without the sample. The subscripts 'object' and 'base' indicate parameters related to the element of interest or base material, while (+) and (-) indicate values for high-energy X-rays after the K-edge and low-energy X-rays before the K-edge, respectively.

According to these equations, obtaining the specific distribution of the element of interest requires knowing mass absorption coefficients for all elements at both energies. However, for a specific sample, element types and proportions are difficult to measure, and introducing theoretical mass absorption coefficients increases data processing errors. Therefore, a uniform background approximation was proposed [26], in which absorption differences of non-target elements at the two energies can be ignored. Accordingly, the distribution of the element of interest is:

$$G_{KES} = \ln\left(\frac{G^{-}_{obj}}{G^{+}_{obj}}\right) - \ln\left(\frac{G^{-}_0}{G^{+}_0}\right) = \Delta\left(\frac{\mu}{\rho}\right)_{obj} \rho_{obj} d \tag{4}$$

where $\Delta(\mu/\rho)_{obj}$ denotes the difference in attenuation coefficient at the two energies, and the numerator represents the grayscale of the KES image after uniform background approximation. Although absorption differences for non-target elements can be ignored under this approximation, an optimized energy range should be selected during KES experiments to maintain the attenuation difference for the element of interest without interference from other elements. According to Eq. 4, a linear relationship exists between the grayscale of KES images after uniform background approximation and the distribution of the element of interest in the sample.

To evaluate image quality during data processing, the contrast-to-noise ratio (CNR) is introduced [35] and expressed as:

$$\mathrm{CNR} = \frac{|\bar{S}_o - \bar{S}_b|}{\sqrt{\sigma_o^2 + \sigma_b^2}} \tag{5}$$

where $\bar{S}_o$ denotes the average grayscale of the object area, $\bar{S}_b$ denotes the average grayscale of the corresponding background area, and σ_o, σ_b denote the standard deviations in the respective regions.

2.2 Experimental Setup

Experiments were conducted at BL13W1, the X-ray Imaging and Biomedical Applications Beamline at the Shanghai Synchrotron Radiation Facility. The experimental setup is illustrated in Fig. 1. X-rays were emitted from a wiggler source and monochromatized by a double-crystal monochromator to modulate the photon energy required for KES imaging, with output X-ray energies in the range of 8–72 keV [36]. The X-ray detector was a Hamamatsu Orca Flash 4.0s CMOS camera with 2048$×2048pixels.CombinedwiththeHamamatsuAA40opticaltransformation(1 : 1), theeffectivepixelsizewas6.5μm.Thedetectorfieldofviewwas13.3mm×$13.3 mm, enabling evaluation of element distribution over relatively large alloy sample areas. The detector was placed 6.5 cm downstream of the sample, with an exposure time of 50 ms per projection.

Prior to experiments, calibration with standard samples for the element of interest was required. In alloy materials, Cu and Ag doping affects structure, density, strength, and shape. We selected copper (Cu) and silver (Ag) for investigation. Attenuation coefficient curves of standard Cu and Ag samples were measured experimentally by scanning photon energy from 8.8 to 9.2 keV in 10 eV steps for Cu, and from 25.3 to 25.5 keV in 10 eV steps for Ag. Based on the obtained attenuation coefficient curves (shown in Appendix A, Supplementary Information), we selected 8.935 keV and 9.005 keV for the Cu K-edge, and 25.37 keV and 25.43 keV for the Ag K-edge for subsequent experiments.

3.1 Different Element Content in One KES Image

The X-ray absorption coefficient of elements is not always continuous with changing X-ray energy. When X-ray energy reaches values that excite electrons at different inner-shell energy levels, the substance exhibits strong X-ray absorption at that energy. This absorption discontinuity is known as the K-edge of the element. Theoretically, the magnitude of this discontinuity is linearly related to the density of the element of interest, meaning the amount of the element in the optical path directly affects the degree of attenuation coefficient change when photon energy is scanned across the K-edge.

We prepared standard samples with known element contents to investigate their linearity with KES image grayscale. During sample preparation, $CuSO_4$ solutions of different concentrations were injected into polyamide 1010 sample tubes with inner and outer diameters of 0.5 mm and 1 mm, respectively. In this $CuSO_4$ solution model, Cu exists as ions. Sample tubes were arranged from left to right in descending density order, corresponding to 9 mg/ml, 8 mg/ml, 7 mg/ml, 6 mg/ml, 5 mg/ml, 4 mg/ml, 3 mg/ml, 2 mg/ml, 1 mg/ml, 0.8 mg/ml, and 0 mg/ml. During image acquisition, the full phantom was accurately positioned within the incident X-ray beam shadow to ensure identical exposure conditions for all samples with different element contents. As mentioned, energies of 8.935 keV and 9.005 keV were selected to record images before and after the Cu K-edge. The KES image and related analysis are shown in Fig. 2.

Figure 2(a) shows the KES image of Cu element content in the phantom. Background noise is visible after K-edge subtraction, particularly around samples with lower Cu concentrations. Additionally, the shadow of sample tubes remains in the subtracted image due to slight X-ray beam movement during acquisition, introducing additional noise for quantitative analysis. This demonstrates that linearity between grayscale and element content deteriorates with noise presence. In alloys, various crystal types exist inside samples after different treatment procedures [37,38], and X-ray scattering from randomly distributed crystals significantly contributes to noisy backgrounds in KES images. Therefore, eliminating noise effects is critical for applying KES X-ray imaging to element content analysis in alloys.

Figure 2(b) shows the grayscale distribution directly obtained from KES images of samples with different Cu concentrations. Linear fitting was performed, and the coefficient of determination (COD, denoted as R^2) was introduced to evaluate distribution linearity, with values closer to 1 indicating better linearity. Figure 2(b) reveals a positive correlation between KES image grayscale and Cu concentration, demonstrating the potential of KES imaging for quantitative element content analysis with large field of view compared to conventional electron methods. However, direct observation shows that grayscale variation with element concentration clearly deviates from linear distribution, with a COD of 0.979 for linear fitting. This implies an overall deviation of 2.1% when using grayscale to evaluate element content, limiting KES method accuracy to 2.1%—insufficient for identifying element distribution, especially when element content in alloys is below 2.1%.

As analyzed above, noise is the primary factor affecting linearity between grayscale and element content. By normalizing pixel grayscale of the element of interest with respect to adjacent background noise, noise effects on linearity can be eliminated. Recently, CNR was introduced to calibrate the nonlinearity of original KES image grayscale. As shown in Eq. 5, signals were normalized by the standard deviation of grayscale in adjacent areas. Substituting original KES image grayscale with corresponding CNR values yields a new element distribution image, as shown in Fig. 2(c). The linearity of the distribution is improved through CNR calibration, with linear fitting yielding a COD of 0.995. This implies that the accuracy of KES imaging for element content evaluation can be significantly improved. It should be noted that accuracy does not indicate resolution limit. Based on experimental results, samples with concentrations as low as 0.8 mg/ml could be resolved, giving KES imaging a sensitivity of 8\$×10^{-4}\$ in this experiment and a dynamic range of 8\$×10$^{\{-4\}-9\times10}${-3}\$. These results provide a reference for evaluating other elements in alloys, such as Sn, Ag, Mo, and Au.

3.2 Element Content in Different KES Images

Based on linearity in KES X-ray imaging, the gray value of standard sample KES images can serve as a benchmark for quantitative analysis of elements in real samples. However, before applying this benchmark, the consistency of linearity between grayscale and element density must be verified across different KES imaging experiments, which is crucial for testing multiple samples.

For quantitative analysis, phantoms with standard samples were prepared to verify experimental consistency. To confirm applicability to other elements, Ag was used. Standard samples with different $AgNO_3$ solution concentrations were filled into polymethyl methacrylate tubes (inner/outer diameter: 2.0 mm/3.0 mm). Three phantoms composed of four standard samples each were designed for verification, with concentrations sequenced in ascending order. Two standard samples of the same concentration in different phantoms enabled comparison between experiments.

Figure 3 shows consistency evaluation results. Figure 3(a) displays KES images of the three phantoms arranged in ascending Ag concentration order. From left to right, $AgNO_3$ concentrations were 0.4 mg/ml, 0.6 mg/ml, 0.8 mg/ml, and 1 mg/ml for phantom No. 1; 1 mg/ml, 2 mg/ml, 4 mg/ml, and 6 mg/ml for phantom No. 2; and 6 mg/ml, 8 mg/ml, 10 mg/ml, and 0 mg/ml for phantom No. 3. The water sample without Ag is not depicted in the KES image, confirming that KES image grayscale solely reflects the element of interest. Grayscale decreased correspondingly with lower Ag concentration, with the lowest concentration of 0.4 mg/ml $AgNO_3$ clearly revealed, implying a detection limit below 4\$×10^{-4}\$ for Ag.

A critical step in KES imaging involves switching energies before and after the element K-edge. At synchrotron beamlines, double-crystal monochromators typically monochromatize and modulate X-ray photon energy. Due to monochromator hysteresis error and beam shift effects, precisely maintaining the same

X-ray beam across experiments is difficult. The vertical profile of synchrotron X-ray beams normally exhibits Gaussian distribution, with output directions at the two K-edge energies deviating slightly. Image subtraction leads to one-way tilting backgrounds, and incident beam pointing errors increase overall grayscale distribution. Beam intensity fluctuations among experiments can cause zero position deviations in different KES images. Before calibrating beam tilting and zero position drift effects, evaluating element content based on grayscale distribution across multiple experiments is difficult.

Figure 3(b) shows grayscale distribution along pixels in KES images. The original grayscale distribution is indicated by the blue line, revealing tilted baselines with varying slopes across different experiments. Grayscale for standard samples with identical concentrations differs between phantoms, particularly for higher element content. Ideally, grayscale profile baselines should be horizontal. We implemented rotation transformation for each profile according to its slope, then reset calibrated baselines to zero position. After these two calibration processes, grayscale profiles for the three phantoms are shown by the red line in Fig. 3(b). After calibration, grayscale for samples with identical concentrations becomes equal across phantoms, and linear correlation between grayscale and element content is observed in each phantom.

For further quantitative analysis, grayscale statistics for all samples across three phantoms were compiled with respect to element content, as shown in Fig. 3(c). Linear fitting yielded a high fitting degree with a COD of 0.994, demonstrating that linearity between grayscale and element content remained consistent across different experiments after elaborate calibration. Therefore, element evaluation of multiple samples using the developed KES imaging method is feasible. The accuracy for element content evaluation based on KES image grayscale was 0.6%. Based on standard samples, the method’ s content resolution was 2\$×10^{-4}\$ with a lower limit of 4\$×10^{-4}\$. Theoretical mass absorption coefficients for typical elements around K-edges are shown in Appendix B (Supplementary Information), and these resolution and limit values indicate that linearity in KES X-ray imaging applies to various doping elements in alloys.

3.3 Alloy Sheet with Uneven Thickness

Strong absorption effects must be considered for alloy samples, requiring sufficiently high X-ray energy around the element K-edge to ensure acceptable transmission. Element Ag was selected for experiments. In typical Sn-Ag-Cu lead-free solders, Ag_3Sn growth and distribution affect alloy mechanical properties and solder joint fatigue life [1]. Moreover, Ag content influences Ag_3Sn formation, making quantitative evaluation of Ag content and distribution in lead-free solder important. Considering strong absorption effects, an alloy sheet was used. During sample preparation, M705 (HIROSAKI) model lead-free solder containing 3% silver was flattened from a 0.3 mm diameter cylinder into a sheet. The detector comprised a 2048\$$\times 2048pixelHAMAMATSUCMOSdetector(model : ORCA -$

$Flash4.0C11440)withanOptiquePeteropticalconversionsystem(model\quad : MICRX016).TheCMOSdetector'sbasicpixelsizewas6.5\mu m, with10\times$ optical magnification yielding an actual pixel size of 0.65 m, enabling higher spatial resolution evaluation of element distribution in alloys.

Figure 4 shows lead-free solder alloy sheet KES imaging results, obtained by subtracting the image acquired at 25.43 keV from that at 25.37 keV after calibration (Fig. 4(a)). Comparison before and after calibration is shown in Appendix C (Supplementary Information). The surface plot of Fig. 4(a) grayscale is shown in Fig. 4(b). Based on KES imaging principles, grayscale value is proportional to the line integral of the linear coefficient for the element of interest, meaning the integral path (e.g., sample thickness) affects results and must be eliminated before evaluating element content. To demonstrate thickness effects, Fig. 4(c) shows the absorption image of lead-free solder at 25.43 keV, an energy just above the Ag K-edge. The images were spliced from two separate measurements, though the border is difficult to discern. Image splicing does not cause abnormal grayscale distribution (Figs. 4(b) and 4(d)), demonstrating feasibility of extending field of view (FOV) by splicing multiple measurements. In this experiment, KES imaging FOV was 1.33 mm$×$2.66 mm at 0.65 m pixel size—a large FOV compared to electron-based in-situ methods while maintaining high spatial resolution. Large FOV analysis capability benefits evaluation of element distribution uniformity across extensive alloy sheet regions.

Figure 4(b) shows a surface plot of Fig. 4(a) grayscale. Based on linearity between grayscale and element content in KES imaging, Fig. 4(b) results represent actual Ag content distribution in flattened lead-free solder, revealing a sinusoidal distribution in the alloy sheet cross-section. Element content obtained by KES imaging reflects the additive effect of element concentration and sample thickness at each point. Rosin is typically injected into alloy hollow cylinders to aid soldering; during sample preparation, rosin was squeezed to both sides, reducing alloy material thickness accordingly. Therefore, the sinusoidal Ag distribution in Fig. 4(b) was obtained. For conventional lead-free solder, Ag doping concentration is completely uniform overall with minute fluctuations, implying thickness variation dominates element content distribution. This deduction is confirmed by grayscale distribution of the absorption image collected at 25.43 keV (above Ag K-edge). As shown in Fig. 4(d), this distribution is similar to Fig. 4(b), though Fig. 4(b) shows higher noise, particularly at thicker alloy locations. This indicates noise also affects element distribution evaluation in alloys. Before calibrating thickness and noise effects, quantitative analysis of element distribution characteristics is difficult.

By normalizing Fig. 4(a) with Fig. 4(c), sample thickness effects can be eliminated, revealing element of interest distribution characteristics as shown in Fig. 5. According to Figs. 5(a) and 5(b), the sinusoidal distribution dominated by alloy thickness is removed, and thickness-normalized content distribution reveals concentration fluctuations in the alloy sheet—pivotal for alloy quality evaluation. The image background is quite noisy upon direct observation (Fig.

5(a)), confirmed by Fig. 5(b) where signals representing element content are submerged in noisy background. As demonstrated in Section 3.1, CNR was introduced to reduce noise effects, with results shown in Figs. 5(c) and 5(d). Figure 5(c) shows efficient noisy background suppression. Figure 5(d) displays the surface plot of Ag concentration distribution in lead-free solder alloy, revealing Ag content fluctuations with limited amplitude above and below an average, indicating fairly uniform Ag distribution. Based on noise-free distribution, cluster phenomena are explicitly revealed in the alloy sheet. As previously indicated, local agglomeration affects solder joint fatigue life.

To quantitatively verify this effect, the average and standard deviation of Ag concentration in Fig. 5(d) were determined as 0.0428$±$0.0011, implying a relative concentration deviation of 2.57%. Overall, Ag distribution uniformity in lead-free solder was fairly good, though local Ag agglomeration relates to alloy mechanical properties and solder joint fatigue life. Therefore, local anomalous Ag distribution was investigated in further detail.

In engineering applications, parameter deviations exceeding twice the standard deviation are typically considered abnormal. Abnormal Ag agglomeration is shown in Fig. 6(a), referring to Ag agglomeration regions with concentration deviation exceeding twice the standard deviation. According to Fig. 6(a), abnormal Ag agglomeration areas are mainly localized in the central part of lead-free solder, with maximum agglomeration size approximately 50 m. In solders, element agglomeration does not directly affect solder joints due to remelting during welding. However, agglomeration with unique sizes exhibits high probability of directly contributing to performance. In this context, the critical value for a unique size is defined as twice the average size corresponding to 2σ, with agglomeration shown in Fig. 6(b) representing typical abnormal agglomeration distribution. Accordingly, the number of Ag agglomerations with concentration deviation exceeding twice the standard deviation and size exceeding twice the average size is 78, potentially contributing to solder joint fatigue life.

4 Conclusion

Doped elements in alloys significantly impact performance. Conventional methods—including destructive techniques such as mass spectrometry and optical spectroscopy, and nondestructive electron-based microscopy—have been extensively applied for alloy element analysis. However, these methods typically require sample surface sputtering for composition analysis or are limited to alloy surfaces due to poor penetration capability. Exploiting high X-ray penetration, the X-ray K-edge subtraction method, which uses KES image grayscale to evaluate element content, exhibits high potential for nondestructive, in situ detection of element content in alloys. However, factors including X-ray scattering in alloys, weak doped element signals in strong absorption backgrounds, and energy modulation of monochromatic X-ray beams severely affect linearity between grayscale and element content, limiting KES method application for alloy element analysis. This study developed methods to calibrate linearity between KES image grayscale and element content to promote KES imaging applications for alloy element analysis.

X-ray scattering and weak doped element signals in strong absorption backgrounds prevent sensitive detection of doped elements in alloys. CNR-based analysis, as opposed to direct KES image grayscale, was proposed to calibrate noise effects on measurement efficiency. Phantom experiments with Cu demonstrated that after normalizing KES image grayscale with adjacent noisy background, CNR values are linearly related to element content, implying that elaborate noise calibration enables CNR-based KES method application for alloy element analysis. Currently, KES imaging of element distribution is a relative measurement, making consistency across multiple sample measurements critical for alloy element analysis. Targeted approaches were developed to calibrate discrepancies between different measurements. Three phantoms with standard sample series were specially designed, and experimental results verified that linear coefficients remained consistent after elaborate calibration. The results indicated a lower content evaluation limit of 4$×10^{-4}$ for Ag, establishing KES imaging applicability for multiple alloy element content measurements.

A lead-free solder alloy sheet with uneven thickness served as a test sample. Splicing two adjacent areas validated measurement consistency by extending KES imaging field of view for alloy element distribution. Uneven sample thickness typically dominates element content, making abnormal element distribution difficult to reveal based on primary KES image grayscale. An absorption image collected at upper K-edge energy was introduced to normalize thickness effects. Results demonstrated that element distribution discrepancies were revealed after elaborate calibration, and quantitative analysis located anomalous element distribution due to local agglomeration. Based on these developed calibration approaches, we conclude that X-ray KES imaging is capable of nondestructive and rapid screening of doped elements in alloys.

Acknowledgements

The authors are grateful to Ya-Nan Fu, Han Guo, Guan-Yun Peng, Fen Tao, Ling Zhang, and Hang Jiang for assistance and fruitful discussions on experiments and data processing. We also thank Ling-Yu Feng, Hui Lu, and Peng-Yuan Qi for guidance in sample preparation.

Author Contributions

Ti-Qiao Xiao conceived this research. Xiao-Lu Ju, Ti-Qiao Xiao, Biao Deng, and Hong-Lan Xie contributed to study design. Material preparation, data collection, and analysis were performed by Xiao-Lu Ju, Biao Deng, Ke Li, Fu-Cheng Yu, and Ti-Qiao Xiao. Xiao-Lu Ju and Ti-Qiao Xiao wrote the first draft. All authors read and approved the final manuscript.

Funding

This work was supported by the National Key Research and Development Program of China (Nos. 2017YFA0403801, 2017YFA0206004, 2018YFC1200204) and the National Natural Science Foundation of China (NSFC) (Nos. 81430087, 11775297, U1932205).

References

1. S.K. Kang, W.K. Choi, D.Y. Shih et al., Ag_3Sn plate formation in the solidification of near-ternary eutectic Sn-Ag-Cu. JOM (2003). http://doi.org/10.1007/s11837-003-0143-6
2. S.K. Kang, D.Y. Shih, D.L. Donald et al., Controlling Ag_3Sn plate formation in near-ternary-eutectic Sn-Ag-Cu solder by minor Zn alloying. JOM 56, 34 (2004). http://doi.org/10.1007/s11837-004-0108-4
3. L.J. Ru, W.Y. Li, W.S. Li et al., Effects of trace cerium addition on microstructure and properties of Cu0.9%Cr alloy. J. Chinese Rare Earth Soc. 36, 106-111 (2018). http://doi.org/10.11785/S1000-4343.20180512
4. S.T. Ma, X. Che, Y. Wang et al., Tensile properties at room and low temperatures of solid-solution treated and aged Al-8Zn-2.5Mg-1.5Cu(-0.15Y) alloys. Heat Treat Met. 44, 174-178 (2019). http://doi.org/10.13251/j.issn.0254-6051.2019.02.032 (in Chinese)
5. C. Yu, D.F. Yin, Effects of trace Ce on strengthening and fracture mechanisms of Al-Li-Cu-Mg-Ag-Zr alloy. Mining and Metallurgical Engineering 33, 116-119 (2013). http://doi.org/10.3969/j.issn.0253-6099.2013.02.030 (in Chinese)
6. B.P. Huang, Z.Q. Zheng, Independent and combined roles of trace Mg and Ag additions in properties, precipitation process and precipitation kinetics of Al-Cu-Li-(Mg)-(Ag)-Zr-Ti alloys. Acta Mater. (1998). http://doi.org/10.1016/S1359-6454(98)00079-2
7. Q.H. Luo, H.Z. Wang, Elemental quantitative distribution and statistical analysis on cross section of stainless steel sheet by laser ablation inductively coupled plasma mass spectrometry. J. Iron Steel Res. Int. 22, 730-737 (2015). http://doi.org/10.1016/S1006-706X(15)30064-9
8. V. Karki, M. Singh, Quantitative depth distribution analysis of elements in high alloy steel using MCs^+-SIMS approach. Int. J. Mass Spectrom. 430, 22-30 (2018). http://doi.org/10.1016/j.ijms.2018.04.001
9. A. Sussulini, J.S. Becker, J.S. Becker, Laser ablation ICP-MS: Application in biomedical research. Mass Spectrom Rev. (2017). http://doi.org/10.1002/mas.21481
10. C. Bich, D. Touboul, A. Brunelle, Biomedical studies by TOF-SIMS imaging. Biointerphases 10, 018901 (2015). http://doi.org/10.1116/1.4901511

11. J. Nuñez, R. Renslow, J.B. Cliff III et al., NanoSIMS for biological applications: Current practices and analyses. Biointerphases (2018). http://doi.org/10.1116/1.4993628 03B301
12. A. Sarkar, V. Karki, S.K. Aggarwal et al., Evaluation of the prediction precision capability of partial least squares regression approach for analysis of high alloy steel by laser induced breakdown spectroscopy. Spectrochim Acta B 108, 8-14 (2015). http://doi.org/10.1016/j.sab.2015.04.002
13. Y. Ishibashi, Rapid analysis of steel by ICP-AES and ICP-MS with laser ablation solid sampling. ISIJ Int. 42, 137-139 (2002). http://doi.org/0915-1559(2002)l:2002<137:RAOSBI>2.0.TX;2-2
14. X.Y. Wei, Y.G. Zheng, Y.S. Zhang et al., Effect of microstructure and element distribution on erosion-corrosion behaviour of an iron base cast alloy. Acta Metall Sin. 030, 91-96 (1994). http://doi.org/10.1007/BF02943514
15. D.B. Kong, C.Q. Li, Formation mechanism of W(Al_8Cu_4Sc) phase in Al-Cu-Li-Sc alloy with high Cu content. Heat Treat. Met. 45, 66-70 (2020). http://doi.org/10.13251/j.issn.0254-6051.2020.02.012
16. M.K. Tiwari, A.K. Singh, K.J.S. Sawhney, Analysis of stainless steel samples by energy dispersive X-ray fluorescence (EDXRF) spectrometry. Bull. Mater. Sci. 24, 633-638 (2001). http://doi.org/10.1007/BF02704012
17. M. Kilo, M. Hund, G. Sauer et al., Reaction induced surface segregation in amorphous CuZr, NiZr and PdZr alloys—an XPS and SIMS depth profiling study. J Alloy Compd. (1996). http://doi.org/10.1016/0925-8388(95)02143-4
18. C.L. Luke, Determination of trace elements in inorganic and organic materials by x-ray fluorescence spectroscopy. Anal Chim Acta. 41, 237-250 (1968). http://doi.org/10.1016/S0003-2670(01)80392-5
19. N.M. Kebonye, K. John, S. Chakraborty et al., Comparison of multivariate methods for arsenic estimation and mapping in floodplain soil via portable X-ray fluorescence spectroscopy. Geoderma (2021). http://doi.org/10.1016/j.geoderma.2020.114792
20. B. Deng, Q. Yang, H.L. Xie et al., First X-ray fluorescence CT experimental results at the SSRF X-ray imaging beamline. Chinese Phys. C 35, 402-404 (2011). http://doi.org/10.1088/1674-1137/35/4/015
21. Q. Yang, B. Deng, W.W. Lv et al., Fast and accurate X-ray fluorescence computed tomography imaging with the ordered-subsets expectation maximization algorithm. J Synchrotron Radiat. (2012). http://doi.org/10.1107/S0909049511052253
22. P.F. Sun, B. Deng, G.H. Du et al., Nondestructive rare earth element imaging of fish teeth from deep sea sediments. X-Ray Spectrom. 44, 442-446 (2015). http://doi.org/10.1002/xrs.2624

23. P.F. Sun, B. Deng, Q. Yang et al., An accelerated OSEM reconstruction algorithm using an accelerating factor for X-ray fluorescence tomography. Nuclear Techniques (2015). http://doi.org/10.11889/j.0253-3219.2015.hjs.38.060201 (in Chinese)
24. B. Deng, G.H. Du, G.Z. Zhou et al., 3D elemental sensitive imaging by full-field XFCT. Analyst. 140, 3521-3525 (2015). http://doi.org/10.1039/c4an02401j
25. B. Jacobson, Dichromatic absorption radiography: Dichromography. Acta Radiol. 39, 437-452 (1953). http://doi.org/10.3109/00016925309136730
26. R.Y. Guo, H.J. Ma, Y.L. Xue et al., K-Edge digital subtraction X-ray imaging for observation of Cu^{2+} adsorption in polymer particles. Acta Optica Sinica 30, 2898-2903 (2010). http://doi.org/10.3788/AOS20103010.2898
27. T. Takeda, Y. Itai, H. Yoshioka et al., Synchrotron radiation cine K-edge energy subtraction coronary arteriography using an iodine filter method. Med. Biol. Eng. Comput. 32, 462-468 (1994). http://doi.org/10.1007/BF02524704
28. A. Suwa, H. Fukagawa, K. Suzuki et al., X-ray K-edge subtraction television system. Jap J Appl Phys. (2014). http://doi.org/10.1143/JJAP.27.1989
29. S. Bayat, G.L. Duc, L. Porra et al., Quantitative functional lung imaging with synchrotron radiation using inhaled xenon as contrast agent. Phys. Med. Biol. 46, 3287-3299 (2001). http://doi.org/10.1088/0031-9155/46/12/315
30. S. Monfraix, S. Bayat, L. Porra et al., Quantitative measurement of regional lung gas volume by synchrotron radiation computed tomography. Phys. Med. Biol. 50, 1-11 (2005). http://doi.org/10.1088/0031-9155/50/1/001
31. L. Porra, L. Degrugilliers, L. Broche et al., Quantitative imaging of regional aerosol deposition, lung ventilation and morphology by synchrotron radiation CT. Sci Rep-UK. 8, 3519 (2018). http://doi.org/10.1038/s41598-018-20986-x
32. H. Elleaume, A.M. Charvet, S. Corde et al., Performance of computed tomography for contrast agent concentration measurements with monochromatic x-ray beams: Comparison of K-edge versus temporal subtraction. Phys. Med. Biol. 47, 3369-3385 (2002). http://doi.org/10.1088/0031-9155/47/18/307
33. D.M.L. Cooper, L.D. Chapman, Y. Carter et al., Three dimensional mapping of strontium in bone by dual energy K-edge subtraction imaging. Phys. Med. Biol. 57, 5777-5786 (2012). http://doi.org/10.1088/0031-9155/57/18/5777

34. L.A. Lehmann, R.E. Alvarez, A. Macovski et al., Generalized image combinations in dual KVP digital radiography. Med. Phys. 8, 659-667 (1981). http://doi.org/10.1118/1.595025
35. G. Lovric, S.F. Barre, J.C. Schittny et al., Dose optimization approach to fast X-ray microtomography of the lung alveoli. J. Appl. Crystallogr. 46, 856-860 (2013). http://doi.org/10.1107/S0021889813005591
36. H.L. Xie, B. Deng, G.H. Du et al., Methodology development and application of X-ray imaging beamline at SSRF. Nucl. Sci. Tech. 31, 102 (2020). http://doi.org/10.1007/s41365-020-00805-7
37. T.M. Tong, J.J. Xu, T.Q. Xiao et al., Evolution of dendrite morphology of a binary alloy under an applied electric current: An in situ observation. Phys. Rev. E 81, 042601 (2010). http://doi.org/10.1103/PhysRevE.81.042601
38. Y.M. Yang, L. Xu, Y.D. Wang et al., Non-destructive identification of unknown minor phases in polycrystalline bulk alloys using three-dimensional X-ray diffraction. Mater Charact. (2017). http://doi.org/10.1016/j.matchar.2016.12.025

Figures

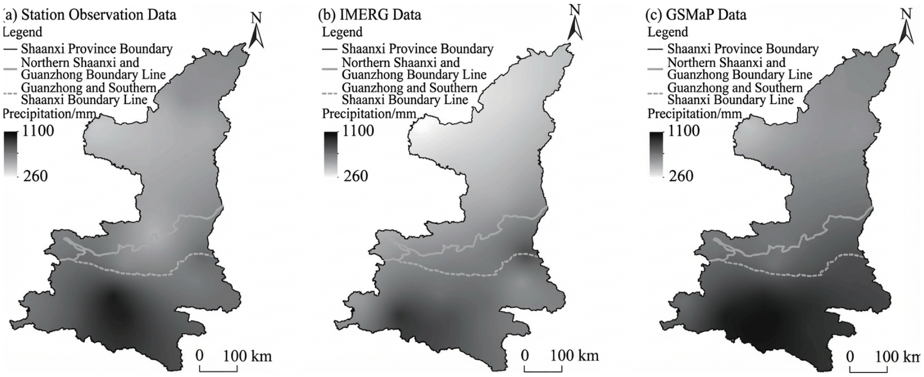

Figure 1: Figure 2

Source: ChinaXiv —Machine translation. Verify with original.

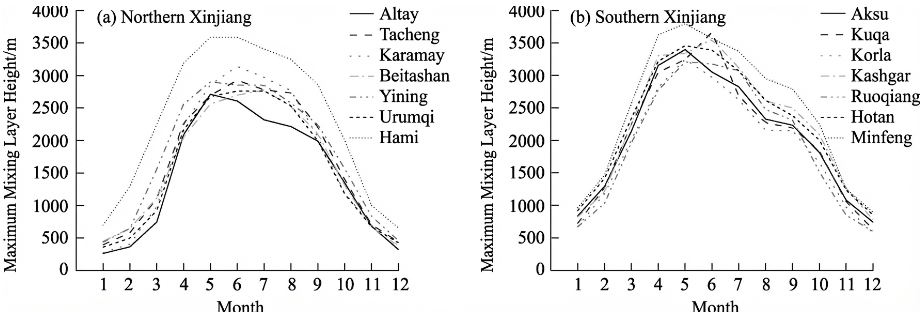

Figure 2: Figure 3

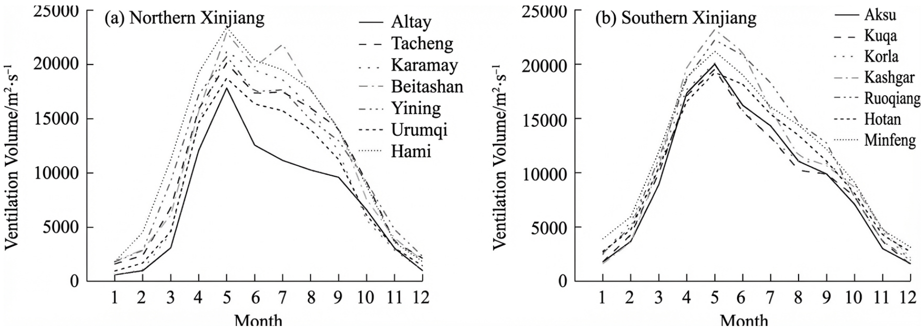

Figure 3: Figure 5